Facile synthesis of chitosan-modified ZnO/ZnFe$_2$O$_4$ nanocomposites for effective remediation of groundwater fluoride

Gautam Kumar Sarma[1] · Raju Sharma[1] · Rosy Saikia[2] · Xavy Borgohain[1] · Saddam Iraqui[1] ·
Krishna Gopal Bhattacharyya[2] · Md. Harunar Rashid[1]

Abstract

This study explores the possibility of developing an eco-friendly adsorbent for effective remediation of groundwater fluoride, a well-known health hazard affecting more than 25 nations on the various continents. A facile and milder approach has been adopted to synthesize chitosan-modified ZnO/ZnFe$_2$O$_4$ nanocomposites. The synthesized materials have been characterized by different spectroscopic, microscopic, and diffractometric techniques. X-ray photoelectron spectroscopy and X-ray diffraction studies have confirmed the formation of pure and highly crystalline ZnO/ZnFe$_2$O$_4$ nanocomposites. The presence of surface-adsorbed chitosan in the modified ZnO/ZnFe$_2$O$_4$ has been confirmed by FT-IR and thermogravimetric analysis. The results from microscopic and BET surface area analysis of ZnO/ZnFe$_2$O$_4$ nanocomposites indicated that chitosan plays a crucial role in modulating the surface morphology and surface properties of the nanocomposites. The nanocomposites exhibit excellent adsorption performance in the remediation of groundwater fluoride. Experimental conditions have been systematically designed to evaluate the optimum adsorption condition for fluoride, and the results have been analyzed with various non-linear models to describe the kinetics and isotherms of adsorption. The adsorption primarily follows Lagergren pseudo-first-order kinetics, and the Langmuir adsorption capacity is varied from 10.54 to 13.03 mg g^{-1} over the temperature range 293–323 K. The thermodynamics study reveals that the adsorption process is endothermic and spontaneous. The mechanism of adsorption has been proposed based on the spectroscopic analysis of the fluoride-loaded adsorbent. The adsorption is non-specific in nature as co-existing anion can reduce its fluoride removal capacity. The effect of the co-existing anions on adsorption of fluoride follows the trend PO$_4^{3-}$ > CO$_3^{2-}$ > SO$_4^{2-}$ > Cl$^-$. The adsorbent can be reused successfully for the 5th consecutive cycles of adsorption-desorption study. This study offers a very promising material for remediation of groundwater fluoride of affected areas.

Keywords Water remediation · Fluoride · Chitosan · ZnO/ZnFe$_2$O$_4$ nanocomposites · Isotherm

Introduction

Fluoride ion is a trace mineral found abundantly in Earth's crust and is classified as a non-biodegradable, persistent pollutant (Roy and Dass 2013; Dehbandi et al. 2018). A small amount of fluoride is necessary for human health, but long-term exposure to fluoride level higher than 1 mg L^{-1} can cause large-scale health problems, like osteosclerosis, thyroid disorder, dental and skeletal fluorosis, and cancer including poor development of an infant's brain (Jagtap et al. 2012; Nur et al. 2014). Considering the severity of the public health risk of fluoride, the World Health Organization (WHO) has set the maximum permissible limit of fluoride in drinking water less than 1.5 mg L^{-1} (WHO 2017). The primary source for fluoride ion contamination in groundwater is the mineralogy of the bedrock, and fluoride is generally released into the groundwater aquifer by slow dissociation of fluoride-containing rocks (Dehbandi et al. 2018). Moreover, many industrial activities like the production of semiconductors, glass manufacturing, ceramic production, metal processing, rubber manufacturing,

✉ Md. Harunar Rashid
    harunar.rashid@rgu.ac.in

[1] Department of Chemistry, Rajiv Gandhi University, Rono Hills, Doimukh, Arunachal Pradesh 791112, India

[2] Department of Chemistry, Gauhati University, Guwahati, Assam 781014, India

and fertilizer production widely utilize fluoride and its compound (Mohammadi et al. 2019). The untreated waste from these industries can contaminate surface water and over time, there is a high probability of groundwater contamination due to leaching. Excess fluoride in groundwater is a worldwide problem and fluorosis can occur anywhere, but the probability is much more prevailing in developing countries like India (Arlappa et al. 2013). Recent reports indicate that in India, 21 states with approximately 66 million people are affected by fluorosis (Adimalla and Qian 2019). Thus, it is essential to bring down the fluoride concentration level in drinking water to an acceptable limit. Accordingly, extensive research has been carried out over the years for the effective removal of fluoride from water, and subsequently, various techniques were developed. Some of the widely used techniques are electrodialysis (Mondal et al. 2018), coagulation (Gan et al. 2019), membrane filtration (Nunes-Pereira et al. 2018), chemical precipitation (Huang et al. 2017), adsorption (Sarma and Rashid 2018; Pillai et al. 2019; Borgohain et al. 2020; Tao et al. 2020), and so on. Among those techniques, adsorption has been recognized as the most popular and promising technology for fluoride removal due to its efficiency, low cost of operation, simplicity, and the ability to choose adsorbent from a wide variety of materials (Jagtap et al. 2012; Kameda et al. 2015). In the recent times, various materials such as bone char (Alkurdi et al. 2020), graphene (Li et al. 2011), chitosan and chitosan-modified nanomaterials (Miretzky and Cirelli 2011; Mohammadi et al. 2019; Ghanbarian et al. 2020), layered double hydroxides (Sarma and Rashid 2018; Liu et al. 2020), activated carbon (Saini et al. 2020), and metal-organic framework (Gao et al. 2019) were used as adsorbents for removal of fluoride from water. Although some of the materials were very effective in the removal of fluoride from water, their high cost of preparation, use of toxic chemicals, and multi-step synthesis approaches limit the applicability. So, the development of an eco-friendly, inexpensive, and efficient adsorbent by a simple synthesis approach for the effective removal of fluoride from both aqueous solution and groundwater is highly desirable.

Literature reports suggest that nanosized metal oxide and hydroxides have great potential to be used as an adsorbent for the removal of various organic and inorganic pollutants from water (Chigondo et al. 2018; Liu et al. 2018; Chaudhary et al. 2019). Among different metal oxides, zinc and iron-based metal oxides have drawn considerable attention from the researchers because both zinc (Zn) and iron (Fe) are environment-friendly, less toxic, and relatively cheap (Sahoo and Hota 2019). As a result, researchers are gradually paying more attention to the synthesis of the mixed metal oxides of Zn and Fe and their subsequent use in different fields. For example, Feng et al. reported the synthesis of magnetic $ZnO/ZnFe_2O_4$ by the microwave combustion method using sodium acetate as fuel. The synthesized $ZnO/ZnFe_2O_4$ was applied for the removal of methylene blue from water in the batch system (Feng et al. 2015). Kuai et al. reported the synthesis of the Ce^{3+}-doped $ZnFe_2O_4$ cluster via the solvothermal method for adsorptive removal of Cr(VI) (Kuai et al. 2013). Amine-functionalized graphene oxide decorated with $ZnO/ZnFe_2O_4$ nanomaterials was reported by Sahoo et al. The composites were synthesized by organic transformation reaction followed by the hydrothermal method and then were used for remediation of Cr(VI) from water (Sahoo and Hota 2019). Wang et al. reported the synthesis of $ZnO/ZnFe_2O_4$ hollow nanocages through a metal-organic framework route in two steps (Wang et al. 2017). These nanocages exhibit enhanced response to acetone with the detection limit of 1 ppm. Yang et al. reported the synthesis of mixed phase porous $ZnO/ZnFe_2O_4$ composite from metal-organic frameworks by microwave irradiation for use as anode materials for LIB (Yang et al. 2017). Chen et al. reported the synthesis of porous $ZnO/ZnFe_2O_4$ particles for photocatalytic application in methylene blue dye degradation (Chen et al. 2017b). Although $ZnO/ZnFe_2O_4$ nanocomposites have been successfully synthesized and subsequently used in different areas, to the best of our knowledge, such nanocomposite has not yet been reported so far for adsorptive removal of fluoride from water. The environment-friendly nature, low toxicity, low cost, and high abundance of Fe and Zn in nature prompted us to choose the mixed metal oxide of Fe and Zn for use as an adsorbent for remediation of groundwater. So, in this manuscript, we report the synthesis of chitosan-modified $ZnO/ZnFe_2O_4$ nanocomposites by a milder co-precipitation method coupled with hydrothermal aging to use them for adsorptive removal of groundwater fluoride.

Experimental section

Materials and method

Materials used

Zinc chloride ($ZnCl_2$), anhydrous ferric chloride ($FeCl_3$), sodium hydroxide (NaOH), SPADNS reagent, and sodium fluoride (NaF) were purchased from Merck, India. Chitosan (200–600 mPa s for 0.5% solution in 0.5% acetic acid at 20 °C) was purchased from TCI, Japan. All the reagents were used as received. All the solutions were prepared in double-distilled water.

Synthesis of $ZnO/ZnFe_2O_4$ nanocomposites

For the synthesis of $ZnO/ZnFe_2O_4$ nanocomposites, we adopted a co-precipitation method coupled with hydrothermal aging following our previously reported method with some modification (Sarma et al. 2019). In a typical synthesis,

anhydrous ferric chloride (0.18 g) and zinc chloride (0.46 g) were dissolved in 140 mL double-distilled water and stirred for 30 min at room temperature (26 °C). To this stirring solution, 10 mL aqueous solution of NaOH (0.72 g) was added dropwise over 10 min from a dropping funnel to achieve a concentration ratio of Fe^{3+}:Zn^{2+}:OH^- = 1:3:18. The suspension formed was stirred for another 60 min at the same temperature. Finally, the reaction mixture containing the precipitate was transferred into 250 mL Teflon-lined autoclave and aged in a preheated air oven at 120 °C for 12 h. After that, the autoclave containing the product was allowed to cool down to room temperature naturally. The final pH of the suspension was recorded to be around 12. The solid precipitate was isolated by centrifugation at 10,000 rpm for 15 min (Remi CPR 24 plus centrifuge). The isolated solid product was purified from any traces of excess reactants by repeated washing with double-distilled water and then rinsed with ethanol. The isolated solid product was dried in vacuum at 60 °C for 12 h and stored in a desiccator for further characterization and use. The sample is designated as Zn-Fe.

In order to synthesize chitosan-modified $ZnO/ZnFe_2O_4$ nanocomposites, a solution of chitosan (20 mL; 2 wt% in 2:98 acetic acid-water solution) was added to the mixed metal solution and the remaining procedure and condition were kept same as in the previous case. The chitosan-modified $ZnO/ZnFe_2O_4$ nanocomposites sample was designated as Zn-Fe-Ch. The synthesized nanocomposites were characterized by different spectroscopic, microscopic, and diffractometric techniques. The details of the characterization techniques are provided in Electronic Supplementary Information (ESI).

Batch adsorption experiments

The fluoride adsorption experiments were carried out in a 100 mL plastic conical flask by mixing a fixed amount of adsorbent with 10 mL of an aqueous fluoride solution. Polypropylene conical flasks were used instead of glass vessels to avoid possible interaction of fluoride with glass as reported earlier (Specht 1956). The mixture was agitated in a thermostatic water bath shaker (NSW, Mumbai, India) at a constant speed of 200 rpm for a pre-determined time interval. The adsorbents were then separated from the mixture by centrifugation at 10,000 rpm for 15 min, and the amount of fluoride remained unadsorbed in the supernatant solution was determined spectrophotometrically (Agilent Cary60 spectrophotometer) using the SPADNS method (Mandal and Mayadevi 2008). The amount of fluoride adsorbed per unit mass of the adsorbent (q_e, mg g^{-1}) and the extent of adsorption (%) were computed using the following equations (Sarma and Rashid 2018):

$$q_e = \frac{C_o - C_t}{m} \tag{1}$$

$$\%\text{Adsorption} = \frac{C_0 - C_t}{C_o} \times 100 \tag{2}$$

where C_o (mg L^{-1}) and C_t (mg L^{-1}) are the initial fluoride concentration and the concentration after adsorption on "m" g of the adsorbent in 1 L solution at a time, t min respectively.

Results and discussion

X-ray diffraction study

Figure 1 shows the X-ray diffraction (XRD) pattern of the as-prepared samples. The diffractogram of both samples Zn-Fe and Zn-Fe-Ch showed the diffraction peaks at 2θ = 31.8, 34.5, 36.3, 47.6, 56.6, 62.9, 66.5, 68.0, 69.1, and 77.0° which are assigned to (100), (002), (101), (102), (110), (103), (200), (112), (201), and (202) planes of ZnO (PDF # 361451). However, the ZnO phases are not pure as some other planes like (220), (400), (422), and (533) corresponding to 2θ = 29.9, 42.7, 52.7, and 73.1° of $ZnFe_2O_4$ (PDF # 221012) (asterisk mark in Fig. 1) were also observed in the diffractogram of both samples. This indicates that highly crystalline mixed phases of $ZnO/ZnFe_2O_4$ are formed in the product. Similar results were also observed earlier by Falak et al. (2017). The XRD results also confirmed that the use of chitosan as an additive has no effect on the crystalline property of the product.

Electron microscopy study

In order to examine the morphological evolution, we recorded the scanning electron microscopy (SEM) images of the
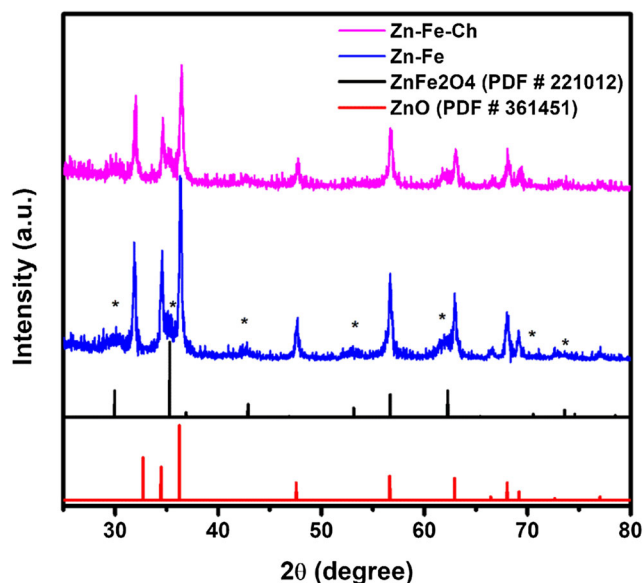

Fig. 1 XRD patterns of $ZnO/ZnFe_2O_4$ nanocomposites prepared both in the absence and in the presence of chitosan

samples. Figure 2a shows the SEM image of sample Zn-Fe which is dominated by rods of geometrical shape either pentagonal or hexagonal. The lengths of these rods are varying from 250 to 400 nm while the width is in the range of 50 to 80 nm. Besides, some assemblies could be observed which are made up of tiny spherical particles. A magnified image of this sample clearly indicated that the rods are of pentagonal geometry (Fig. 2b). The SEM image of the chitosan-modified sample (Zn-Fe-Ch) shown in Fig. 2c also shows the presence of rod-shaped structures that are mostly flattened and no geometrical shape could be observed. Also, due to the presence of chitosan, the image is darkened which might be due to possible charging effect during e-beam irradiation. The lengths of these flat rods are also slightly shorter than those observed in the case of sample Zn-Fe. This might be due to the blocking of some of the faces by chitosan during their growth and thereby restrict the formation properly.

Further, to study the morphological evolution, transmission electron microscopy (TEM) images were recorded from both samples. The TEM image recorded from sample Zn-Fe (Fig. S1a in the ESI) confirmed the presence of rod-shaped structures along with tiny spherical nanoparticles, while the TEM image of sample Zn-Fe-Ch (Fig. S1b in the ESI) shows the presence of undefined shape of the nanocomposites.

FTIR spectroscopy

In order to verify the attachment of chitosan on the ZnO/ZnFe$_2$O$_4$ nanostructures modified with chitosan, we recorded the Fourier transform infrared (FTIR) spectra of both samples. The FTIR spectrum of the unmodified ZnO/ZnFe$_2$O$_4$ nanocomposite (Fig. 3) shows the presence of peaks at 3434 and 1640 cm^{-1} which are due to the –OH stretching and bending mode of surface adsorbed water (Mohseni-Bandpi et al. 2015). The strong peaks at 1562 and 1407 cm^{-1} are the characteristic peak of ZnO (Ullah and Dutta 2008). The peaks below 580 cm^{-1} are due to metal–oxygen (M–O) bond vibration. The FTIR spectrum of chitosan-modified ZnO/ZnFe$_2$O$_4$ nanocomposite showed additional peaks apart from those
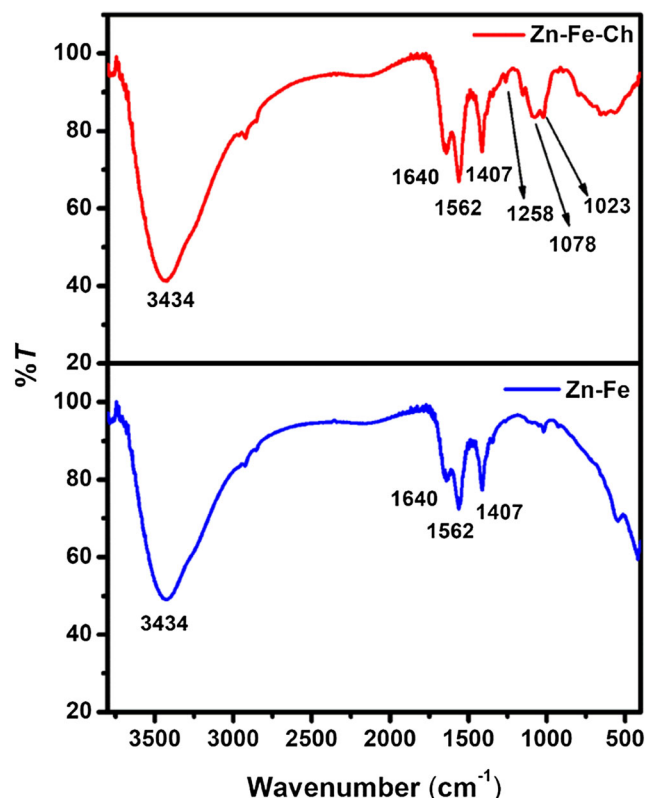

Fig. 3 FTIR spectra of the prepared ZnO/ZnFe$_2$O$_4$ nanocomposites

observed in the spectrum of the unmodified ZnO/ZnFe$_2$O$_4$. Peaks appeared at 1078 and 1023 cm^{-1} can be attributed to C–OH bond stretching (Mohseni-Bandpi et al. 2015). Another peak appeared at 1258 cm^{-1} confirms the presence of an amino group of chitosan on the sample (Thakur et al. 2016). Also, the peak due to M–O vibrations disappears in the chitosan-modified ZnO/ZnFe$_2$O$_4$ nanocomposite, and instead, a group of weakly intense peaks appeared at 607 cm^{-1}. This suggests that both the metals, Zn and Fe, have interacted with the functional groups of chitosan. Also, it is evident that chitosan molecules are anchored on the surface of chitosan-modified ZnO/ZnFe$_2$O$_4$ nanocomposite.
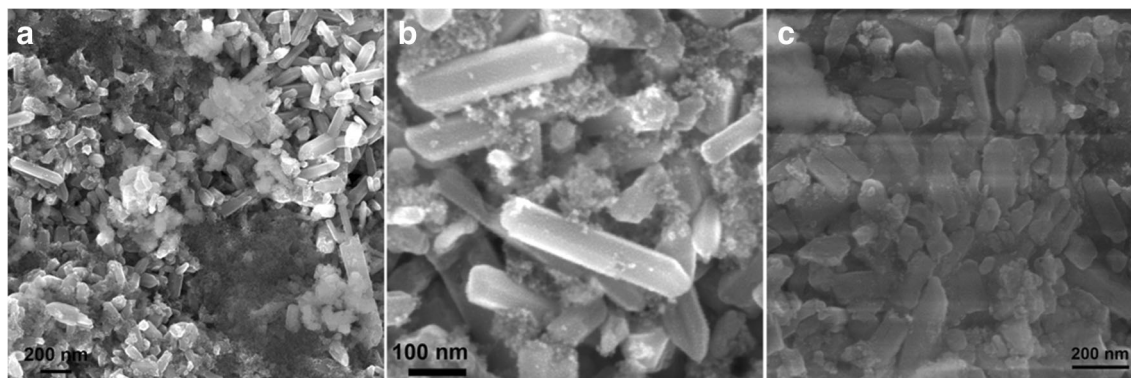

Fig. 2 FESEM images of the as-prepared ZnO/ZnFe$_2$O$_4$ nanocomposites. **a** Low and **b** high magnification images of sample Zn-Fe and **c** sample Zn-Fe-Ch

Thermogravimetric analysis

Further, to confirm the amount of surface-adsorbed chitosan on the chitosan-modified ZnO/ZnFe$_2$O$_4$ nanocomposite and to study the thermal stability, thermogravimetric analysis (TGA) was carried out on both samples. The thermogram of sample Zn-Fe (Fig. S2 in the ESI) shows a weight loss of 5 wt% up to temperature 300 °C which is attributed to the removal of adsorbed moisture by the sample, whereas sample Zn-Fe-Ch exhibited sharp decomposition at 70 and 293 °C with a total weight loss of 25% which correspond to again the removal of surface-adsorbed water molecules. As chitosan being macromolecules might also adsorb a significant amount of water, so the weight loss is much higher than the previous sample. Another sharp decomposition occurred at the

temperature range of 350 to 500 °C which corresponds to 22 wt% weight losses. This decomposition is associated with the degradation of chitosan moieties. This clearly indicates that a significant amount of chitosan is anchored on the surface of sample Zn-Fe-Ch.

X-ray photoelectron spectroscopy

To understand the surface composition and chemical state of the prepared materials, X-ray photoelectron spectroscopy (XPS) study was carried out. The binding energies in the XPS analysis were corrected for specimen charging by setting the binding energy of carbon (C 1s) at 284.6 eV. The XPS survey spectrum shown in Fig. 4a indicates the presence of Zn 2p, Fe 2p, and O 1s on the surface of the Zn-Fe sample
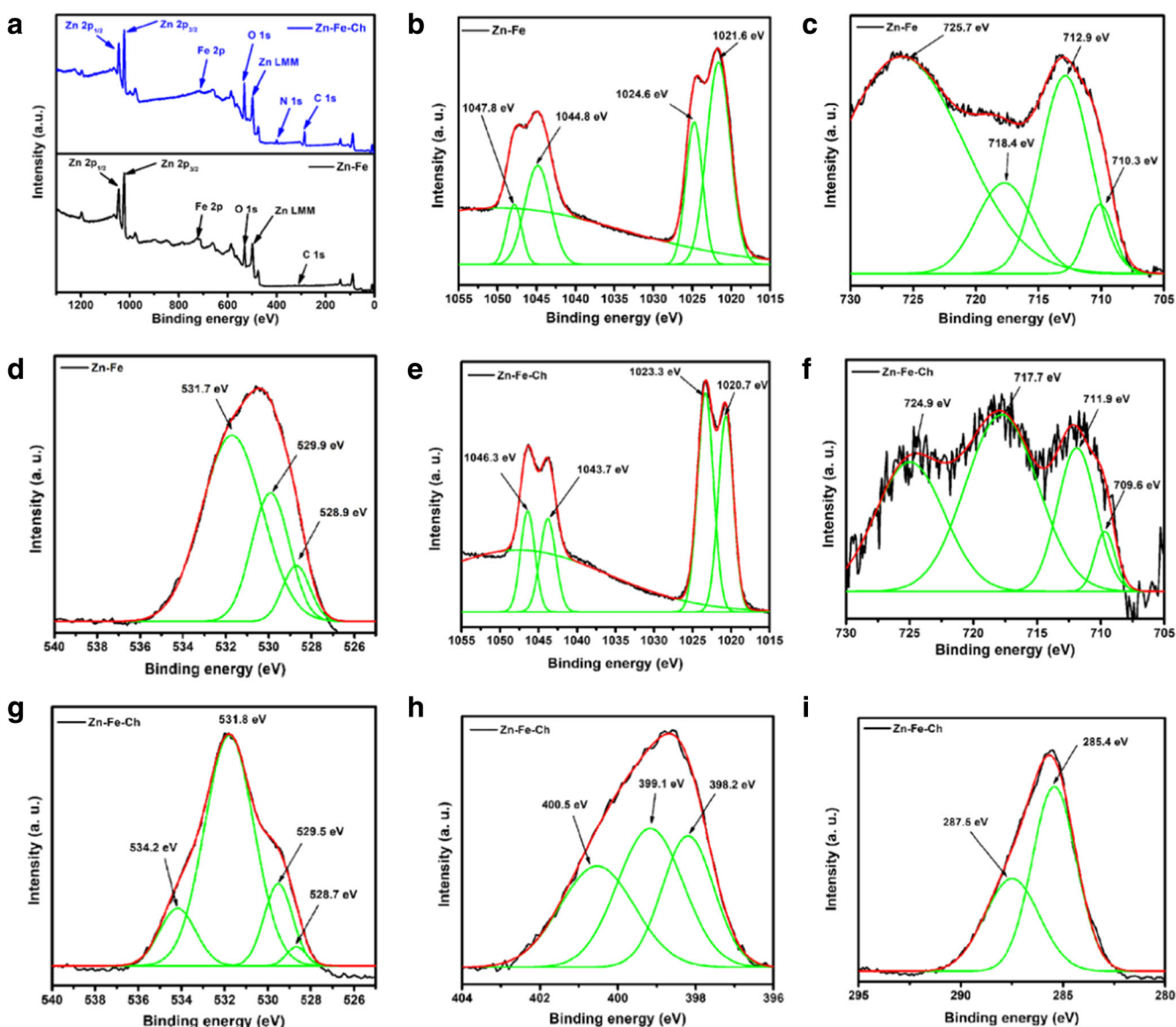

Fig. 4 XPS spectra of the different as-prepared ZnO/ZnFe$_2$O$_4$ nanocomposites: **a** survey spectra for both samples Zn-Fe and Zn-Fe-Ch. High resolution spectra of **b** Zn 2p, **c** Fe 2p, **d** O 1s region of sample Zn-Fe and **e** Zn 2p, **f** Fe 2p, **g** O 1s, **h** N 1s, and **i** C 1s region for sample Zn-Fe-Ch

suggesting very high purity of the synthesized material. The core-level Zn 2p XPS spectrum and the corresponding fitted data of sample Zn-Fe (Fig. 4b) shows four peaks at ~1021.7, 1024.6, 1044.8, and 1047.8 eV. The peaks at ~1044.8 eV (Zn $2p_{1/2}$) and ~1021.7 eV (Zn $2p_{3/2}$) can be assigned to Zn^{2+} ions in ZnO (Chen et al. 2016a; Yang et al. 2017). The other two peaks at ~1047.8 (Zn $2p_{1/2}$) and ~1024.6 eV (Zn $2p_{3/2}$) could be due to the presence of Zn^{2+} in octahedral sites of $ZnFe_2O_4$ in the product (Gawas et al. 2013; She et al. 2017). Usually, in bulk $ZnFe_2O_4$, the Zn^{2+} ions have a preference for the tetrahedral site in the spinel structure. Due to the size reduction, a considerable concentration of Zn^{2+} ions occupies the octahedral sites resulting in slightly higher binding energies for its 2p peak (Gawas et al. 2013). The XPS spectrum of core-level Fe 2p showed two broad peaks (Fig. 4c) located at ~725.7 ($2p_{1/2}$) and 713.1 ($2p_{3/2}$) eV with a satellite peak of Fe $2p_{3/2}$ at around ~719.4 eV. These peaks correspond to the presence of Fe in the Fe(III) state in the product (Thakur et al. 2016). The presence of a satellite peak further supports the absence of the Fe_3O_4 phase in the composite (Kaloti and Kumar 2016). The Fe $2p_{3/2}$ peak can further be fitted into two peaks at ~712.7 and ~710.1 eV which corresponds to the presence of Fe^{3+} ions in both octahedral and tetrahedral sites of $ZnFe_2O_4$ respectively (Chen et al. 2017a). These observations prove that the $ZnFe_2O_4$ component in the nanocomposite has a partial inverse spinel structure (Chen et al. 2017a). The high-resolution XPS spectrum (Fig. 4d) of O 1s showed a broad peak at ~530.9 eV, which can be fitted into three peaks at ~528.9, 529.9, and 531.7 eV. These peaks correspond well to lattice oxygen O^{2-} from Zn-O and Fe-O linkages in metal–oxygen framework, O^{2-} in the oxygen-deficient regions resulting in a higher number of defect sites, and absorbed oxygen species (i.e., OH, H_2O, or carbonate species) respectively (Hou et al. 2015; Chen et al. 2017a).

The $ZnO/ZnFe_2O_4$ nanocomposites synthesized in presence of chitosan, Zn-Fe-Ch, showed all the expected characteristic XPS peaks for Fe 2p, Zn 2p, O 1s, C 1s, and N 1s in the survey scan spectrum (Fig. 4a). The core-level spectra of Zn 2p (Fig. 4e) and Fe 2p (Fig. 4f) remained almost the same as those of sample Zn-Fe. However, the peaks are shifted to lower binding energy by ~1.0–1.5 eV for Zn 2p and ~0–1.0 eV for Fe 2p. This shifting of the fitted XPS peaks suggests possible interaction of Zn and Fe in $ZnO/ZnFe_2O_4$ with chitosan molecule. All the original O 1s XPS peaks due to the presence of lattice oxygen O^{2-} from Zn-O and Fe-O linkages in metal–oxygen framework, O^{2-} in the oxygen-deficient regions, and absorbed oxygen species (i.e., OH, H_2O, or carbonate species) are present in sample Zn-Fe-Ch (Fig. 4g) with very minimal shifting of 0–0.2 eV suggesting no interaction between these O species and chitosan. A new peak at ~534.1 eV in sample Zn-Fe-Ch can be assigned to the carbonyl oxygen of the acetamido group present in chitosan (Kaloti and Kumar 2016). The presence of N 1s and highly intense C 1s

peak in sample Zn-Fe-Ch further confirmed the attachment of chitosan molecules on the surface of $ZnO/ZnFe_2O_4$ nanocomposites in sample Zn-Fe-Ch. The broad peak of N 1s (Fig. 4h) at binding energy ~397.4 eV could be fitted into three peaks at 400.5, 399.1, and 398.2 eV. The peaks at 398.2 and 398.3 eV can be assigned to the free $-NH_2$ and NH_2-O respectively. The other peak at ~400.5 eV arises due to possible NH_2–metal upon chelating with the nanocomposite (Kaloti and Kumar 2016). The high-resolution spectrum of C 1s (Fig. 4i) displays a broad peak at 285.6 eV which can be fitted into two peaks at the binding energies 285.4 and 287.5 eV. These peaks are attributed to C-O/C-N and C-O-C/C=O respectively (Kaloti and Kumar 2016).

N_2 gas adsorption-desorption study

Surface characteristics of the synthesized materials play a crucial role in the adsorption study. To get an insight into the surface characteristics, N_2 gas adsorption-desorption study was undertaken (Fig. S3 in the ESI) at 77 K after degassing the samples at 120 °C for 4 h. The shape of the isotherm for both samples could be categorized into type IV with an H3 hysteresis loop which is quite typical for mesoporous material with plate-like particles with slit-shaped pores (Sing et al. 1985). Multipoint Brunauer–Emmett–Teller (BET) surface area of samples Zn-Fe and Zn-Fe-Ch was found to be 5.523 and 73.235 m^2 g^{-1} respectively. This confirmed that the addition of chitosan significantly enhanced the surface area of the nanocomposites. Pore size analysis from the Barrett–Joyner–Halenda (BJH) plots shows that there is a 10-fold increase in the pore volume due to the modification of Zn-Fe by chitosan as pore volume increased from 0.014 cm^3 g^{-1} in sample Zn-Fe to 0.143 cm^3 g^{-1} in sample Zn-Fe-Ch. It is also clear from the BJH plots (Fig. S3 in the ESI) that in sample Zn-Fe-Ch, an additional pore is present which exhibits an additional peak centered around 5.2 nm along with the peak at 3–4 nm appeared in both samples. Since the pore size lies in the range 2–50 nm, we assumed these nanostructures as mesoporous (Sing et al. 1985).

Adsorption kinetics

Adsorption kinetics is one of the very important aspects to consider while designing an adsorption system to determine the time required for attaining adsorption equilibrium. The effect of contact time on adsorption of fluoride was studied using an initial fluoride concentration of 10 mg L^{-1} with the constant adsorbent amount of 1 g L^{-1} at 303 K. The results (Fig. S4 in the ESI) indicated that initially, the adsorption is fast with almost 50% adsorption taking place within 60 min, and the equilibrium is reached approximately within 240 min. The adsorption results were fitted to the nonlinear form of two of the widely used kinetic models, namely the Lagergren

pseudo-first-order model (eq. 3) and pseudo-second-order model (eq. 4) to understand its kinetic behavior (Hameed and El-Khaiary 2008a).

$$q_t = q_e\left(1-e^{-k_1 t}\right) \tag{3}$$

$$q_t = \frac{q_e^2 k_2 t}{1 + q_e k_2 t} \tag{4}$$

where q_e (mg g^{-1}) and q_t (mg g^{-1}) are the amounts adsorbed per unit mass at equilibrium and at any time, t (min) respectively; k_1 is the first-order rate coefficient (min^{-1}); and k_2 is the rate constant of pseudo-second-order (g mg^{-1} min^{-1}). The plots for both the models are shown in Fig. 5, and the estimated data are shown in Table S1 in the ESI. The comparison of the R^2 value suggested that the Lagergren pseudo-first ($R^2 = 0.98$–0.97) and pseudo-second-order ($R^2 = 0.99$–0.99) both give a good fit. However, a comparison of experimental q_e and q_e obtained from the fitted models suggested that Lagergren pseudo-first-order kinetics can be used to describe the adsorption kinetics for both the adsorbent at 30 °C (Sattarfard et al. 2018).

In batch mode, constant shaking was involved during the adsorption process; therefore, there are possibilities of diffusion processes being the rate-determining step. To verify this, the adsorption data were fitted to Webber's pore diffusion model (Hameed and El-Khaiary 2008a). The model is defined by the equation:

$$q_t = k_i t^{0.5} + C \tag{5}$$

where k_i is the pore diffusion parameter (mg g^{-1} min$^{-0.5}$) and q_t (mg g^{-1}) is the amount adsorbed at time t (min) and C is the resistance to mass transfer in the external liquid film. From Eq. (5), we can say that a plot of q_t vs. $t^{0.5}$ would be a straight line if pore diffusion is the rate-determining step. The pore diffusion plot (Fig. S5a in the ESI) shows the multilinear curve

with two linear segments. The regression data (Table S1 in the ESI) clearly indicated that the intercepts from the first linear segment for both samples Zn-Fe and Zn-Fe-Ch are very close to zero but not exactly zero as demanded by the model. Thus, we can assume that pore diffusion is not the overall rate to control the adsorption process. Thus, there is the probability of liquid film diffusion instead of pore diffusion in the early stage of the adsorption. To prove this assumption, we also fitted the data to the Boyd film diffusion model (Eq. 6) (Boyd et al. 1947). The presence of two k_i values in the intraparticle plot (Table S1 in the ESI) means that the diffusion of fluoride ion on Zn-Fe and Zn-Fe-Ch occurs in two very distinct pores, say macropore and micropores. The decrease observed in the value of k_i is due to the diffusion of fluoride ion from macropore to mesopore as the path available for diffusion decreases with a decrease in the size of the pore (Hameed and El-Khaiary 2008a).

$$F = 1-\left(\frac{6}{\pi^2}\right)\sum_{n=1}^{\infty}\left(\frac{1}{n^2}\right)e^{-n^2 \mathrm{B}t} \tag{6}$$

where $F = q_t/q_e$ is the fractional attainment of equilibrium, at different times, t; and Bt is a function of F. q_t and q_e are the amount adsorbed at time t (min) and at equilibrium respectively. But the direct calculation of B is not possible from Eq. (6), so Reichenberg (1953) derived the following approximation by applying Fourier transform and integration:

$$\text{For } F > 0.85,\ \mathrm{B}t = -0.4977-\ln(1-F) \tag{7}$$

$$\text{For } F < 0.85,\ \mathrm{B}t = \left(\sqrt{\pi}-\sqrt{\pi-\left(\frac{\pi^2 F}{3}\right)}\right)^2 \tag{8}$$

The value of B obtained from the plot can be used to calculate the effective diffusion coefficient, D_i (cm^2/s), from the equation:
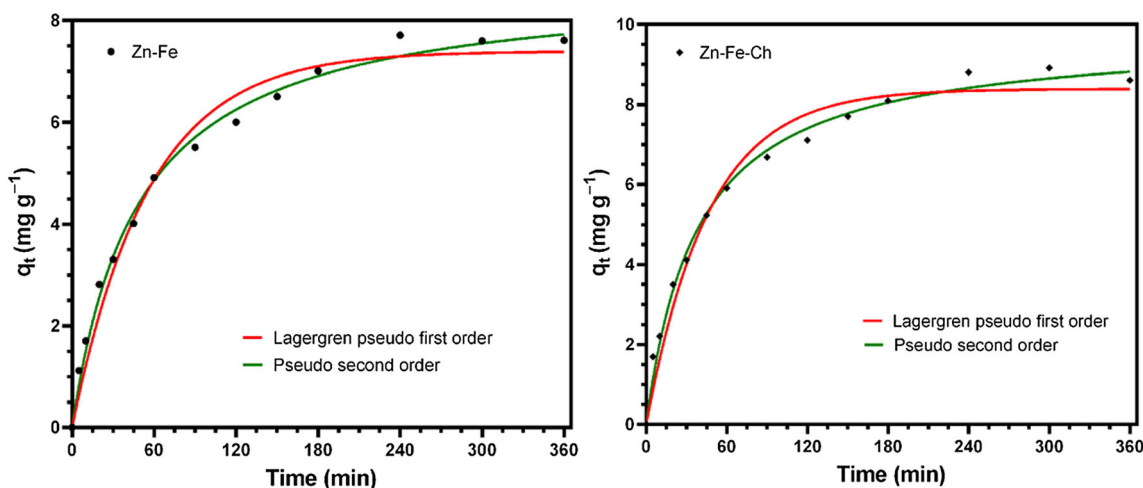

Fig. 5 The experimental and nonlinear fitted kinetic plots for samples **a** Zn-Fe and **b** Zn-Fe-Ch

$$B = \frac{\pi^2 D_i}{r^2} \qquad (9)$$

Here, r is the radius of the absorbent particle assuming a spherical shape.

The Boyd plot of Bt vs t for the first 45 min for both Zn-Fe and Zn-Fe-Ch (Fig. S5b in the ESI) shows that the plots for the initial part of the adsorption are linear but the line does not pass through the origin as the intercept is varied in the range − 0.016 to − 0.02 with a slope in the range of 0.008 to 0.009 (Table S1 in the ESI). Therefore, we assume that external mass transfer is the rate-determining step at the initial stage of the adsorption (Hameed and El-Khaiary 2008b). But, since the intercept is very close to zero, but not exactly zero, we cannot ignore the probability of pore diffusion in the overall adsorption mechanism (Hameed and El-Khaiary 2008a).

Adsorption isotherm

To understand the adsorption type and to get an insight into the relationship between adsorbate and adsorbent, the equilibrium data were fitted into the nonlinear form of Freundlich, Langmuir, and Dubinin-Radushkevich (D-R) isotherm models (Foo and Hameed 2010). The nonlinear forms of these equations are:

$$\text{Freundlich isotherm}: q_e = K_F \, C_e^{1/n} \qquad (10)$$

$$\text{Langmuir isotherm}: q_e = \frac{q_m b C_e}{1 + b C_e} \qquad (11)$$

$$\text{D-R isotherm}: q_e = q_s e^{-k_{ad} \varepsilon^2} \qquad (12)$$

where C_e is the equilibrium concentration of the fluoride ion in aqueous solution (mg L^{-1}); q_e is the equilibrium concentration of the fluoride ion in the solid phase (mg g^{-1}); K_F (mg$^{1-1/n}$ L$^{1/n}$ g^{-1}) and n are the Freundlich coefficients; q_m (monolayer adsorption capacity) and b (equilibrium coefficient) are Langmuir coefficients; q_s is the theoretical saturation capacity (mg g^{-1}). The parameter k_{ad} is the D-R isotherm constant (mol^2 k^{-1} J^{-2}). The parameter ε can be correlated as (Liu and Liu 2008):

$$\varepsilon = RT \ln\left(1 + \frac{1}{C_e}\right) \qquad (13)$$

where R, T, and C_e represent the gas constant (8.314 J mol^{-1} K^{-1}), temperature (K), and adsorbate equilibrium concentration (mg L^{-1}) respectively. The mean sorption energy, E, which is the free energy of transfer of 1 mol of solute, from infinity (bulk solution) to the surface of adsorbent, is given by (Liu and Liu 2008),

$$E = \frac{1}{\sqrt{2k_{ad}}} \qquad (14)$$

The E (kJ mol^{-1}) value provides valuable information about adsorption characteristics. When the value of E lies between 8 and 16 kJ mol^{-1}, the adsorption process is considered to be chemical in nature, whereas if the value is less than 8 kJ mol^{-1}, the interaction is depicted as physical in nature. Figure 6 showed the fitting of all the isotherm models into the experimental data obtained at 30 °C, and the calculated isotherm parameters are shown in Table 1. The R^2 values for both Zn-Fe and Zn-Fe-Ch showed better fit to the Freundlich isotherm (0.97–0.99) than either Langmuir (0.91–0.95) or D-R (0.89–0.91) isotherms in the temperature range 293–323 K. The Freundlich adsorption capacities, K_F, varied in the range 6.2–6.6 for sample Zn-Fe and 6.9–7.8 for sample Zn-Fe-Ch in the studied temperature range 293–323 K (Table 1). The calculated n values are also greater than 1 suggesting favorable adsorption. The Langmuir isotherm parameter b varied in the range 0.71 to 1.4, suggesting a favorable formation of the fluoride-adsorbent complex for both samples Zn-Fe and Zn-
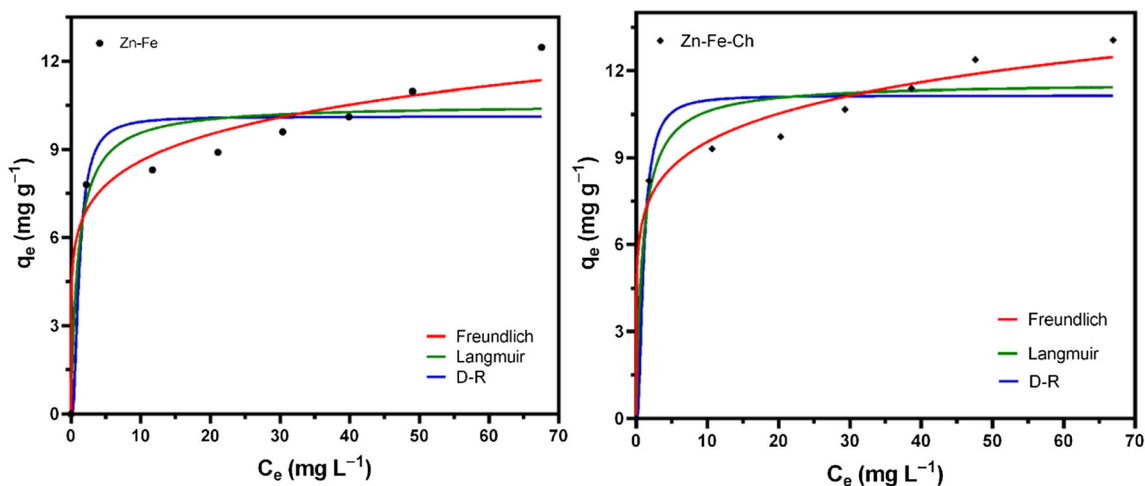

Fig. 6 Experimental and the nonlinear fitted plots of three isotherm models of fluoride adsorption on the as-prepared ZnO/ZnFe$_2$O$_4$ nanocomposites at 30 °C

Table 1 Isotherm data for adsorption of fluoride onto samples Zn-Fe and Zn-Fe-Ch (Adsorbent dose 1.0 g L^{-1}, initial fluoride concentration 10 to 80 mg L^{-1}, pH 6.1 (as-prepared fluoride solution))

Adsorbent	Isotherm	Isotherm parameters	293 K	303 K	313 K	323 K
Zn-Fe	Freundlich	K_F (mg$^{1-1/n}$ L$^{1/n}$ g^{-1})	6.2	6.5	6.4	6.6
		n	6.9	6.8	6.1	6.1
		R^2	0.97	0.98	0.98	0.99
	Langmuir	q_m (mg g^{-1})	10.54	11.19	11.77	12.19
		b (L mg^{-1})	0.98	0.90	0.75	0.71
		R^2	0.91	0.93	0.92	0.94
	D-R	q_s (mg g^{-1})	10.12	10.71	11.16	11.53
		$k_{ad} \times 10^7$ (mol^2 k^{-1} J^{-2})	3.3	3.3	3.4	3.5
		R^2	0.89	0.91	0.89	0.91
		E (kJ mol^{-1})	5.38	5.37	5.26	5.22
Zn-Fe-Ch	Freundlich	K_F (mg$^{1-1/n}$ L$^{1/n}$ g^{-1})	6.9	7.4	7.3	7.8
		n	7.1	7.4	6.4	7.0
		R^2	0.98	0.98	0.99	0.99
	Langmuir	q_m (mg g^{-1})	11.58	12.04	13.03	13.03
		b (L mg^{-1})	1.08	1.45	0.83	1.27
		R^2	0.93	0.92	0.95	0.94
	D-R	q_s (mg g^{-1})	11.15	11.65	12.40	12.58
		$k_{ad} \times 10^7$ (mol^2 k^{-1} J^{-2})	2.7	1.7	2.9	1.7
		R^2	0.91	0.90	0.92	0.92
		E (kJ mol^{-1})	5.89	7.43	5.77	7.59

Fe-Ch in the studied temperature range of 293–323 K. However, as the values are quite low, it is unlikely that the fluoride-adsorbent complex would be a stable one. Langmuir monolayer adsorption capacity, q_m, increases with an increase in temperature from 293 to 323 K. Monolayer adsorption capacity of samples Zn-Fe and Zn-Fe-Ch increased by ~13% and ~11% respectively when the adsorption temperature was increased from 293 to 323 K. Also, the chitosan-modified ZnO/ZnFe$_2$O$_4$ nanocomposites showed a satisfactory ~9% increase in fluoride adsorption capacity compared with unmodified ZnO/ZnFe$_2$O$_4$ nanocomposites at 293 K. A comparison of Langmuir adsorption capacities of some other reported chitosan-based adsorbents for removal of fluoride from water (Table S2 in the ESI) indicated that the removal of fluoride is difficult and traditionally, the performance of most of the adsorbents is very low. Therefore, we claim that the performance of the current system for fluoride removal is satisfactory compared with similarly reported adsorbents. Also, a 9% increase in the adsorption capacity by modification with chitosan is quite significant in this study.

The D-R isotherm model is most useful for calculating the energy involved in the adsorption process. The D-R coefficients, q_s and k_{ad}, could be computed from the nonlinear plot and after converting the unit from mg L^{-1} to mmol L^{-1} by considering the atomic weight of fluorine. The D-R theoretical saturation capacity, q_s, is in the range 10.12 to 11.53 mg g^{-1} for Zn-Fe and 11.15 to 12.58 mg g^{-1} for Zn-Fe-Ch in the temperature range of the study. The saturation capacity values

increases with increase in temperature for both the adsorbents. The D-R isotherm constant, k_{ad}, is in the range of 1.65×10^{-7} to 3.487×10^{-7} mol^2 kJ^{-2} (Table 1). The mean sorption energy, E, was found to vary in the range 5.21 to 7.58 kJ mol^{-1} for both Zn-Fe and Zn-Fe-Ch at the temperature range of 293 to 323 K. This implied that the interaction between fluoride and the adsorbent is not strong enough and mere physical forces holding them together. In order to confirm this fact, zeta potential value of sample Zn-Fe-Ch was recorded (Fig. S6 in the ESI) which gives an average zeta potential of 0.0 mV. This result further confirmed that the interaction between the adsorbent and adsorbate is not electrostatic rather physical adsorption takes place predominantly.

Effect of adsorbent loading

The effect of adsorbent dose on fluoride adsorption was examined by varying the amount of the adsorbent in the range 1.0 to 5.0 g L^{-1} for 240 min, the equilibrium time at 303 K with an initial fluoride concentration of 15 mg L^{-1}. It was observed that, with an increase in adsorbent dose from 1.0 to 5.0 g L^{-1}, the %adsorption of fluoride increases from 56.66 to 99.08% for sample Zn-Fe and from 60.70 to 99.33% for sample Zn-Fe-Ch respectively (Fig. S7a in the ESI). This increase in %adsorption is the result of an increase in available adsorption sites. However, the opposite trend was observed when the amount adsorbed per unit mass (q_e) was plotted against the adsorbent dose (Fig. S7b in the ESI). That is the value of q_e

decreases from 8.50 to 2.48 mg L^{-1} with an increase in the adsorbent dose of sample Zn-Fe and from 9.11 to 2.48 mg L^{-1}for sample Zn-Fe-Ch. So, we assume that some of the adsorption sites are not available for the fluoride ion at higher adsorbent loading because of possible coagulation of the adsorbent making less room for the available fluoride ions. This might be the reason for the decrease in adsorption per unit mass even though there is a net overall increase in the percentage of adsorption.

Adsorption thermodynamics

The effects of temperature (293–323 K) on adsorption of fluoride on samples Zn-Fe and Zn-Fe-Ch are shown in Fig. S8 in the ESI. In this temperature range, the increase in % adsorption of fluoride on sample Zn-Fe is very small and nearly constant after 303 K. However, for sample Zn-Fe-Ch, this increase is slightly higher (from 82.09 to 86.87%) in the temperature range 293–323 K. It is important to know the thermodynamic parameters to get an insight into the changes occurring in the internal energy due to adsorption. More importantly, it also gives an idea about the spontaneity of an adsorption process. Here, the thermodynamic adsorption parameters, enthalpy change, $\Delta H°$, entropy change, $\Delta S°$, and Gibbs free energy change, $\Delta G°$, were computed with the help of the following equations:

$$\Delta G° = \Delta H° - T\Delta S° \tag{15}$$

$$\Delta G° = -RT\ln K \tag{16}$$

The combined form of Eqs. (15) and (16) gives:

$$\ln K = \frac{\Delta S°}{R} - \frac{\Delta H°}{RT} \tag{17}$$

where R is the universal gas constant (8.314 J K^{-1} mol^{-1}); T is the absolute temperature; K represents the adsorption constants of the Langmuir isotherm fit, b in L mg^{-1} which is modified to dimensionless quantity following the procedure suggested by Lima et al. (Lima et al. 2019).

The changes in adsorption enthalpy, $\Delta H°$, was found to be 9.16 and 0.68 kJ mol^{-1} for samples Zn-Fe and Zn-Fe-Ch respectively (Table 2). The positive $\Delta H°$ values suggest the adsorption process be endothermic. However, as $\Delta H° < 25$ kJ mol^{-1}, the adsorption process is mainly physisorption (Liu and Liu 2008). This verified the earlier observation made

with the help of mean sorption energy, E, from D-R isotherm. The positive values of entropy of adsorption, $\Delta S°$ indicated increased randomness in the solid-liquid interface during adsorption. It is reported that $\Delta S°$ values determine if an adsorption process is associative or dissociative in nature. Generally, a value of $\Delta S°$ greater than -10.0 J K^{-1} mol^{-1} supports a dissociative mechanism (Abbasizadeh et al. 2014). In this study, the positive values of $\Delta S°$ indicated that the adsorption of fluoride onto the adsorbent favors dissociative mechanism. The negative values of Gibbs free energy, $\Delta G°$, for the adsorbents under consideration suggest thermodynamically favorable fluoride-adsorbent interaction.

Adsorption mechanism

In order to understand the adsorption mechanism, we recorded the XPS and FTIR spectra of the adsorbent before (Zn-Fe-Ch) and after (Zn-Fe-Ch-F) fluoride adsorption. FTIR spectra of Zn-Fe-Ch-F showed only minor changes compared with Zn-Fe-Ch (Fig. S9 in the ESI). The M–O stretching vibration of Zn-Fe-Ch has slightly shifted to a higher frequency. This increase in frequency might be due to the interaction of more electronegative fluoride with the metals resulting in the shift of M–O stretching frequency to a slightly higher frequency. A more substantial shift was also observed for the peak at 1078 cm^{-1} due to the C-O stretching mode to 1094 cm^{-1}. This indicated the possibility of interaction of fluoride with the carbon atom of the chitosan molecule. A new peak was also observed in fluoride-adsorbed sample at 1258 cm^{-1} which is attributed to the aryl ring C-F stretch mode of vibration. The probable carbon-fluorine interaction was further supported by the XPS (Fig. S10 in the ESI). The presence of F 1s peak in the survey spectrum of sample Zn-Fe-Ch-F (Fig. S10a in the ESI) proved the adsorption of fluoride on the surface of chitosan-modified ZnO/ZnFe$_2$O$_4$ nanocomposite. The F 1s peak can be fitted into two peaks (Fig. S10b in the ESI) centered at 688.2 and 690.4 eV which are characteristic for C–F and C–F$_2$ bonds respectively (Fan et al. 2018).

Reusability of the adsorbent

To investigate the feasibility of using the adsorbent, namely Zn-Fe-Ch, in successive batches, the desorption-readsorption study of fluoride was carried out in a systematic manner. A suspension of 3 g L^{-1} of sample Zn-Fe-Ch

Table 2 Thermodynamic data for adsorption of fluoride on samples Zn-Fe and Zn-Fe-Ch (adsorbent dose 1.0 g L^{-1}, initial fluoride concentration range 10–80 mg L^{-1}, pH 6.1 (as-prepared fluoride solution))

Adsorbent	$\Delta H°$ (kJ mol^{-1})	$\Delta S°$ (J K^{-1} mol^{-1})	$\Delta G°$ (kJ mol^{-1})			
			293 K	303 K	313 K	323 K
Zn-Fe	9.158	50.56	-5.65	-6.16	-6.66	-7.17
Zn-Fe-Ch	0.678	80.75	-22.98	-23.78	-24.59	-25.40

was used to adsorb fluoride from a 10 ml solution with a fluoride concentration of 30 ppm. After the adsorption, the solid materials were isolated by centrifugation. The isolated solid was washed with a 10 mL of 5% NaOH solution in an ultrasonic bath for 15 min. Then, the adsorbent was again centrifuged and washed with distilled water in a spinning vortex to remove the excess NaOH. The purified solid was then used as an adsorbent for fluoride from a fresh solution of 10 mL of 10 mg L^{-1} fluoride solution. The process was repeated for 5 cycles and the variation of %adsorption is shown in Fig. 7. We are delighted to note that the adsorption performance of the nanocomposites decreases slightly after the first cycle and then becomes almost steady thereafter up to the 5th cycle. So, we strongly believe that the adsorption performance of chitosan-modified ZnO/ZnFe$_2$O$_4$ nanocomposites is very much persistent for successive uses thereby making it economically viable for industrial use.

Fluoride removal from natural groundwater sample

In order to examine the efficiency of the prepared adsorbent for removal of fluoride from the real field sample, we collected water samples from a fluoride affected area of Karbi Anglong district of Assam, India. The water quality parameters are listed in Table S3 in the ESI. Since the fluoride concentration is very high (14 mg L^{-1}) in the sample, we performed the adsorbent dose variation study up to 240 min (equilibrium time of the study) to find the minimum amount of adsorbent needed to bring the fluoride concentration value to the permissible limit of 1.5 mg L^{-1}. The results shown in Fig. 8 clearly indicated that 6.0 g L^{-1} of the adsorbent (sample Zn-Fe-Ch) is needed to bring the fluoride level down to
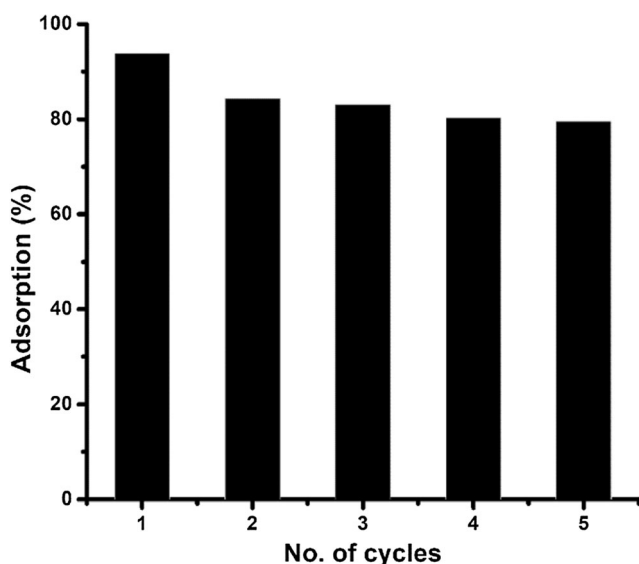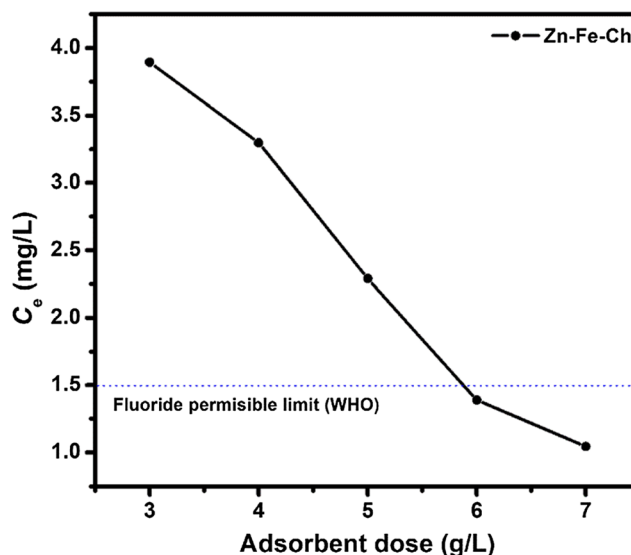

Fig. 8 Plot showing the variation of C_e (remaining concentration of fluoride after 240 min in mg L^{-1}) with the adsorbent dose for sample Zn-Fe-Ch

1.5 g L^{-1}. For field water, the adsorbent amount required is higher than the synthetic samples due to the presence of various co-existing anions in the field sample which competes with fluoride ion for the adsorption sites.

Effect of co-existing anions

The study of the removal of fluoride from groundwater has shown that the presence of co-existing anions can interfere with the adsorption performance. Therefore, to better understand what type of anion has a greater impact, we evaluated the effects of co-existing anions such as Cl$^-$, SO$_4^{2-}$, CO$_3^{2-}$, and PO$_4^{3-}$ individually on the adsorption of fluoride at pH 6.7 with sample Zn-Fe-Ch. The experiments were carried out in batch mode with an initial fluoride concentration of 10 mg L^{-1}, and the concentration of individual anion was fixed at 100 mg L^{-1} with an adsorbent dose of 1.0 g L^{-1}. The effect of the anions on adsorption of fluoride follows the trend PO$_4^{3-}$ > CO$_3^{2-}$ > SO$_4^{2-}$ > Cl$^-$. This particular trend actually follows the Z/r (charge/radius in nm) values for the individual anions. Here, Cl$^-$ has the lowest impact on the adsorption of fluoride. It also has the lowest Z/r value of 5.52. Moreover, Cl$^-$ is considered a low-affinity ligand and since its adsorption occurs via weak bonds of outer-sphere complexation with the active site of the adsorbent material reducing its interference (Huang et al. 2011). The Z/r values of other anions follow the order PO$_4^{3-}$: $3/0.238 = 12.61$ > CO$_3^{2-}$: $2/0.178 = 11.23$ > SO$_4^{2-}$ = $2/0.258 = 7.70$ > Cl$^-$: $1/0.181 = 5.52$. Therefore, all the divalent anion in this study competes with fluoride ion for the active site of the adsorbent due to high Z/r value. Zhang et al. reported similar observations for fluoride removal using Ce-Zr oxide nanosphere encapsulated calcium alginate

Fig. 7 Histogram showing the variation of %adsorption in different cycles for sample Zn-Fe-Ch

(Chen et al. 2016b). Figure S11 in the ESI shows the effect of co-existing anions on the fluoride removal.

Conclusion

Chitosan-modified $ZnO/ZnFe_2O_4$ nanocomposites have been prepared by the co-precipitation method coupled with hydrothermal aging in an aqueous medium. XRD and XPS studies confirmed the presence of ZnO and $ZnFe_2O_4$ in the nanocomposites where the $ZnFe_2O_4$ phase has an inverse spinel structure. The presence of chitosan does not affect the crystalline property of the product but increases the BET surface area to a large extent from 5.523 to 73.235 m^2 g^{-1}. The chitosan-modified $ZnO/ZnFe_2O_4$ nanocomposite exhibits better adsorption capacity compared with that prepared in the absence of chitosan. The kinetics studies showed that the adsorption process is complex and both the adsorbents primarily follow the Lagergren pseudo-first-order model with the diffusion process playing significant role in different stages of adsorption without being the rate-determining step. Langmuir monolayer adsorption capacity increases with an increase in temperature from 293 to 323 K for both the modified and unmodified adsorbents. The adsorption process is endothermic and spontaneous, and the presence of co-anions in water reduces the fluoride adsorption capacity of the adsorbent in the order PO_4^{3-} > CO_3^{2-} > SO_4^{2-} > Cl^-. This reduction in the adsorption capacity is in accordance with the Z/r ratio of the anion. Even though the adsorbent is not selective, it is very effective for the remediation of groundwater fluoride demonstrating its practical real-life applicability. Being a water-stable biopolymer, chitosan possesses unique properties such as biocompatibility, biodegradability, bio-functionality, and non-toxicity, and the relatively higher adsorption capacity of the chitosan-modified adsorbent with the low-cost and low-energy synthesis method can make it an attractive material for water purification. The adsorbent can also be used up to the 5th cycle of the adsorption-desorption process with minimal loss of 15% fluoride adsorbing capacity.

Compliance with ethical standards

Conflict of interest The authors declare that they have no conflict of interest.

References

Abbasizadeh S, Keshtkar AR, Mousavian MA (2014) Sorption of heavy metal ions from aqueous solution by a novel cast PVA/TiO_2 nanohybrid adsorbent functionalized with amine groups. J Ind Eng Chem 20:1656–1664. https://doi.org/10.1016/j.jiec.2013.08.013

Adimalla N, Qian H (2019) Hydrogeochemistry and fluoride contamination in the hard rock terrain of central Telangana, India: analyses of its spatial distribution and health risk. SN Appl Sci 1:202. https://doi.org/10.1007/s42452-019-0219-8

Alkurdi SSA, Al-Juboori RA, Bundschuh J, Bowtell L, McKnight S (2020) Effect of pyrolysis conditions on bone char characterization and its ability for arsenic and fluoride removal. Environ Pollut 262: 114221. https://doi.org/10.1016/j.envpol.2020.114221

Arlappa N, Aatif Qureshi I, Srinivas R (2013) Fluorosis in India: an overview. Int J Res Dev Health 1:97–102

Borgohain X, Boruah A, Sarma GK, Rashid MH (2020) Rapid and extremely high adsorption performance of porous MgO nanostructures for fluoride removal from water. J Mol Liq 305:112799. https://doi.org/10.1016/j.molliq.2020.112799

Boyd GE, Adamson AW, Myers LS (1947) The exchange adsorption of ions from aqueous solutions by organic zeolites. II. Kinetics. J Am Chem Soc 69:2836–2848. https://doi.org/10.1021/ja01203a066

Chaudhary M, Rawat S, Jain N, Bhatnagar A, Maiti A (2019) Chitosan-Fe-Al-Mn metal oxyhydroxides composite as highly efficient fluoride scavenger for aqueous medium. Carbohydr Polym 216:140–148. https://doi.org/10.1016/j.carbpol.2019.04.028

Chen D, Shen W, Wu S, Chen C, Luo X, Guo L (2016a) Ion exchange induced removal of Pb(II) by MOF-derived magnetic inorganic sorbents. Nanoscale 8:7172–7179. https://doi.org/10.1039/c6nr00695g

Chen H, Liu W, Qin Z (2017a) $ZnO/ZnFe_2O_4$ nanocomposite as a broad-spectrum photo-Fenton-like photocatalyst with near-infrared activity. Catal Sci Technol 7:2236–2244. https://doi.org/10.1039/c7cy00308k

Chen L, Zhang K, He J, Cai X-G, Xu W, Liu J-H (2016b) Performance and mechanism of hierarchically porous Ce–Zr oxide nanospheres encapsulated calcium alginate beads for fluoride removal from water. RSC Adv 6:36296–36306. https://doi.org/10.1039/c6ra01337f

Chen M, Liu D, Deng Y, Fu W, Zou H, Liang F (2017b) Tailoring the porosity of $ZnO/ZnFe_2O_4$ composites for photocatalytic applications. Ceram Int 43:16027–16031. https://doi.org/10.1016/j.ceramint.2017.08.148

Chigondo M, Paumo HK, Bhaumik M, Pillay K, Maity A (2018) Rapid high adsorption performance of hydrous cerium-magnesium oxides for removal of fluoride from water. J Mol Liq 265:496–509. https://doi.org/10.1016/j.molliq.2018.06.015

Dehbandi R, Moore F, Keshavarzi B (2018) Geochemical sources, hydrogeochemical behavior, and health risk assessment of fluoride in an endemic fluorosis area, central Iran. Chemosphere 193:763–776. https://doi.org/10.1016/j.chemosphere.2017.11.021

Falak P, Hassanzadeh-Tabrizi SA, Saffar-Teluri A (2017) Synthesis, characterization, and magnetic properties of $ZnO-ZnFe_2O_4$ nanoparticles with high photocatalytic activity. J Magn Magn Mater 441:98–104. https://doi.org/10.1016/j.jmmm.2017.05.044

Fan K et al (2018) Towards enhanced tribological performance as water-based lubricant additive: selective fluorination of graphene oxide at mild temperature. J Colloid Interface Sci 531:138–147. https://doi.org/10.1016/j.jcis.2018.07.059

Feng J et al (2015) Synthesis of magnetic $ZnO/ZnFe_2O_4$ by a microwave combustion method, and its high rate of adsorption of methylene blue. J Colloid Interface Sci 438:318–322. https://doi.org/10.1016/j.jcis.2014.10.009

Foo KY, Hameed BH (2010) Insights into the modeling of adsorption isotherm systems. Chem Eng J 156:2–10. https://doi.org/10.1016/j.cej.2009.09.013

Gan Y, Wang X, Zhang L, Wu B, Zhang G, Zhang S (2019) Coagulation removal of fluoride by zirconium tetrachloride: performance evaluation and mechanism analysis. Chemosphere 218:860–868. https://doi.org/10.1016/j.chemosphere.2018.11.192

Gao Q, Xu J, Bu X-H (2019) Recent advances about metal-organic frameworks in the removal of pollutants from wastewater. Coord Chem Rev 378:17–31. https://doi.org/10.1016/j.ccr.2018.03.015

Gawas UB, Verenkar VMS, Barman SR, Meena SS, Bhatt P (2013) Synthesis of nanosize and sintered $Mn_{0.3}Ni_{0.3}Zn_{0.4}Fe_2O_4$ ferrite and their structural and dielectric studies. J Alloys Compd 555:225–231. https://doi.org/10.1016/j.jallcom.2012.12.054

Ghanbarian M, Ghanbarian M, Mahvi AH, Tabatabaie T (2020) Enhanced fluoride removal over $MgFe_2O_4$–chitosan–CaAl nanohybrid: response surface optimization, kinetic and isotherm study. Int J Biol Macromol 148:574–590. https://doi.org/10.1016/j.ijbiomac.2020.01.143

Hameed BH, El-Khaiary MI (2008a) Equilibrium, kinetics and mechanism of malachite green adsorption on activated carbon prepared from bamboo by K_2CO_3 activation and subsequent gasification with CO_2. J Hazard Mater 157:344–351. https://doi.org/10.1016/j.jhazmat.2007.12.105

Hameed BH, El-Khaiary MI (2008b) Kinetics and equilibrium studies of malachite green adsorption on rice straw-derived char. J Hazard Mater 153:701–708. https://doi.org/10.1016/j.jhazmat.2007.09.019

Hou L, Lian L, Zhang L, Pang G, Yuan C, Zhang X (2015) Self-sacrifice template fabrication of hierarchical mesoporous bi-component-active $ZnO/ZnFe_2O_4$ sub-microcubes as superior anode towards high-performance lithium-ion battery. Adv Funct Mater 25:238–246. https://doi.org/10.1002/adfm.201402827

Huang H, Liu J, Zhang P, Zhang D, Gao F (2017) Investigation on the simultaneous removal of fluoride, ammonia nitrogen and phosphate from semiconductor wastewater using chemical precipitation. Chem Eng J 307:696–706. https://doi.org/10.1016/j.cej.2016.08.134

Huang Y-H, Shih Y-J, Chang C-C (2011) Adsorption of fluoride by waste iron oxide: the effects of solution pH, major coexisting anions, and adsorbent calcination temperature. J Hazard Mater 186:1355–1359. https://doi.org/10.1016/j.jhazmat.2010.12.025

Jagtap S, Yenkie MK, Labhsetwar N, Rayalu S (2012) Fluoride in drinking water and defluoridation of water. Chem Rev 112:2454–2466. https://doi.org/10.1021/cr2002855

Kaloti M, Kumar A (2016) Synthesis of chitosan-mediated silver coated γ-Fe_2O_3 ($Ag-\gamma-Fe_2O_3@Cs$) superparamagnetic binary nanohybrids for multifunctional applications. J Phys Chem C 120:17627–17644. https://doi.org/10.1021/acs.jpcc.6b05851

Kameda T, Oba J, Yoshioka T (2015) Recyclable Mg–Al layered double hydroxides for fluoride removal: kinetic and equilibrium studies. J Hazard Mater 300:475–482. https://doi.org/10.1016/j.jhazmat.2015.07.023

Kuai S, Zhang Z, Nan Z (2013) Synthesis of Ce^{3+} doped $ZnFe_2O_4$ self-assembled clusters and adsorption of chromium(VI). J Hazard Mater 250–251:229–237. https://doi.org/10.1016/j.jhazmat.2013.01.074

Li Y et al (2011) Adsorption of fluoride from aqueous solution by graphene. J Colloid Interface Sci 363:348–354. https://doi.org/10.1016/j.jcis.2011.07.032

Lima EC, Hosseini-Bandegharaei A, Moreno-Piraján JC, Anastopoulos I (2019) A critical review of the estimation of the thermodynamic parameters on adsorption equilibria. Wrong use of equilibrium constant in the van't Hoof equation for calculation of thermodynamic parameters of adsorption. J Mol Liq 273:425–434. https://doi.org/10.1016/j.molliq.2018.10.048

Liu J, Xie L, Yue X, Xu C, Lu X (2020) Removal of fluoride and hardness by layered double hydroxides: property and mechanism. Int J Environ Sci Technol 17:673–682. https://doi.org/10.1007/s13762-019-02457-6

Liu R, Chi L, Wang X, Sui Y, Wang Y, Arandiyan H (2018) Review of metal (hydr)oxide and other adsorptive materials for phosphate removal from water. J Environ Chem Eng 6:5269–5286. https://doi.org/10.1016/j.jece.2018.08.008

Liu Y, Liu Y-J (2008) Biosorption isotherms, kinetics and thermodynamics. Sep Purif Technol 61:229–242. https://doi.org/10.1016/j.seppur.2007.10.002

Mandal S, Mayadevi S (2008) Adsorption of fluoride ions by Zn-Al layered double hydroxides. Appl Clay Sci 40:54–62. https://doi.org/10.1016/j.clay.2007.07.004

Miretzky P, Cirelli AF (2011) Fluoride removal from water by chitosan derivatives and composites: a review. J Fluor Chem 132:231–240. https://doi.org/10.1016/j.jfluchem.2011.02.001

Mohammadi E et al (2019) Synthesis of carboxylated chitosan modified with ferromagnetic nanoparticles for adsorptive removal of fluoride, nitrate, and phosphate anions from aqueous solutions. J Mol Liq 273:116–124. https://doi.org/10.1016/j.molliq.2018.10.019

Mohseni-Bandpi A, Kakavandi B, Kalantary RR, Azari A, Keramati A (2015) Development of a novel magnetite-chitosan composite for the removal of fluoride from drinking water: adsorption modeling and optimization. RSC Adv 5:73279–73289. https://doi.org/10.1039/c5ra11294j

Mondal R, Pal S, Bhalani DV, Bhadja V, Chatterjee U, Jewrajka SK (2018) Preparation of polyvinylidene fluoride blend anion exchange membranes via non-solvent induced phase inversion for desalination and fluoride removal. Desalination 445:85–94. https://doi.org/10.1016/j.desal.2018.07.032

Nunes-Pereira J et al (2018) Highly efficient removal of fluoride from aqueous media through polymer composite membranes. Sep Purif Technol 205:1–10. https://doi.org/10.1016/j.seppur.2018.05.015

Nur T, Loganathan P, Nguyen TC, Vigneswaran S, Singh G, Kandasamy J (2014) Batch and column adsorption and desorption of fluoride using hydrous ferric oxide: solution chemistry and modeling. Chem Eng J 247:93–102. https://doi.org/10.1016/j.cej.2014.03.009

Pillai P, Lakhtaria Y, Dharaskar S, Khalid M (2019) Synthesis, characterization, and application of iron oxyhydroxide coated with rice husk for fluoride removal from aqueous media. Environ Sci Pollut Res. https://doi.org/10.1007/s11356-019-05948-8

Reichenberg D (1953) Properties of ion-exchange resins in relation to their structure. III. kinetics of exchange. J Am Chem Soc 75:589–597. https://doi.org/10.1021/ja01099a022

Roy S, Dass G (2013) Fluoride contamination in drinking water-a review. Resour Environ 3:53–58. https://doi.org/10.5923/j.re.20130303.02

Sahoo SK, Hota G (2019) Amine-functionalized GO decorated with $ZnO-ZnFe_2O_4$ nanomaterials for remediation of Cr(VI) from water. ACS Appl Nano Mater 2:983–996. https://doi.org/10.1021/acsanm.8b02286

Saini A, Maheshwari PH, Tripathy SS, Waseem S, Dhakate SR (2020) Processing of rice straw to derive carbon with efficient de-fluoridation properties for drinking water treatment. J Water Process Eng 34:101136. https://doi.org/10.1016/j.jwpe.2020.101136

Sarma GK, Khan A, El-Toni AM, Rashid MH (2019) Shape-tunable $CuO-Nd(OH)_3$ nanocomposites with excellent adsorption capacity in organic dye removal and regeneration of spent adsorbent to reduce secondary waste. J Hazard Mater 380:120838. https://doi.org/10.1016/j.jhazmat.2019.120838

Sarma GK, Rashid MH (2018) Synthesis of Mg/Al Layered double hydroxides for adsorptive removal of fluoride from water: a mechanistic and kinetic study. J Chem Eng Data 63:2957–2965. https://doi.org/10.1021/acs.jced.8b00242

Sattarfard R, Behnajady MA, Eskandarloo H (2018) Hydrothermal synthesis of mesoporous TiO_2 nanotubes and their adsorption affinity toward Basic Violet 2. J Porous Mater 25:359–371. https://doi.org/10.1007/s10934-017-0447-5

She X, Zhang Z, Baek M, Yong K (2017) Elevated photoelectrochemical activity of $FeVO_4/ZnFe_2O_4/ZnO$ branch-structures via slag assisted-

synthesis. RSC Adv 7:16787–16794. https://doi.org/10.1039/c7ra00812k

Sing KSW, Everett DH, Haul RAW, Moscou L, Pierotti RA, Rouquerol J, Siemieniewska T (1985) Reporting physisorption data for gas/solid systems with special reference to the determination of surface area and porosity. Pure Appl Chem 57:603–619

Specht RC (1956) Interaction of fluoride ions and ground glass. Anal Chem 28:1015–1017. https://doi.org/10.1021/ac60114a026

Tao W, Zhong H, Pan X, Wang P, Wang H, Huang L (2020) Removal of fluoride from wastewater solution using Ce-AlOOH with oxalic acid as modification. J Hazard Mater 384:121373. https://doi.org/10.1016/j.jhazmat.2019.121373

Thakur G, Singh A, Singh I (2016) Chitosan-montmorillonite polymer composites: formulation and evaluation of sustained release tablets of aceclofenac. Sci Pharm 84:603–617. https://doi.org/10.3390/scipharm84040603

Ullah R, Dutta J (2008) Photocatalytic degradation of organic dyes with manganese-doped ZnO nanoparticles. J Hazard Mater 156:194–200. https://doi.org/10.1016/j.jhazmat.2007.12.033

Wang X, Zhang S, Shao M, Huang J, Deng X, Hou P, Xu X (2017) Fabrication of ZnO/ZnFe$_2$O$_4$ hollow nanocages through metal organic frameworks route with enhanced gas sensing properties. Sensors Actuators B Chem 251:27–33. https://doi.org/10.1016/j.snb.2017.04.114

WHO (2017) Guidelines for drinking-water quality (2017) World Health Organization:631

Yang X, Xue H, Yang Q, Yuan R, Kang W, Lee C-S (2017) Preparation of porous ZnO/ZnFe$_2$O$_4$ composite from metal organic frameworks and its applications for lithium ion batteries. Chem Eng J 308:340–346. https://doi.org/10.1016/j.cej.2016.09.071